Quantum confinement effects above the fundamental band gap in $HgTe/Hg_{0.3}Cd_{0.7}Te$ heterostructures studied by resonant Raman scattering near the E_1 edge

R. Atzmüller, M. Rösch, G. Schaack, and C. R. Becker
Physikalisches Institut der Universität Würzburg, Am Hubland, D-97074 Würzburg, Germany
(Received 9 April 1996; revised manuscript received 14 August 1996)

We have investigated the resonance enhancement of the Raman scattering efficiency of the TO, LO, and 2LO phonon processes in a series of $HgTe/Hg_{0.3}Cd_{0.7}Te$ heterostructures with (001), (110), and (111) orientations at the E_1 band gap. In addition, interface modes and localized defect modes have been observed. Quantum confinement effects could be detected at the E_1 transition in this system and a second (excited) electronic subband was verified. For the (110) and (111) orientations, the electronic degeneracy at the E_1 gap is lifted and two resonance maxima appear, in accordance with the transverse effective mass ($0.145m_0$) derived for a (001) grown sample. Selection rules for Raman backscattering from zinc-blende heterostructures in the vicinity of the E_1 gap have been derived for deformation-potential and Fröhlich intraband coupling and are compared with experimental results. [S0163-1829(96)04848-5]

I. INTRODUCTION

Quantum confinement effects of charge carriers in low-dimensional systems based on III-V and II-VI semiconductors are of central importance both in fundamental research and with respect to applications in sophisticated devices. Whereas most structures rely on carriers confined at the fundamental (E_0) band gap at or near the center (Γ) of the Brillouin zone (BZ), only in a few cases the possibility of lateral quantization has been investigated in other regions of the BZ.[1–4] IV-VI lead chalcogenides have their narrowest direct band gap at the L points of the BZ (E_1) with an eightfold degeneracy in the bulk (many valley semiconductor), and confinement effects have been verified in this case (Refs. 3 and 4, and references therein). In II-VI materials, on the other hand, quantum-size related shifts in optical transitions at the E_1 gap have been observed in CdTe glass filters, containing semiconducting crystallites of diameter size around 5 to 15 nm isolated in a glass matrix.[2] In the group of IV-IV materials, Ge/Si quantum wells and superlattices have been studied in this respect.[5,6] Resonant Raman scattering in hexagonal quasi-two-dimensional InSe near the M_1 critical point has also been observed and interpreted.[7] Similar results have been obtained in III-V GaAs/InAs and GaAs/AlAs superlattices.[8,9]

Heterostructures (HS's) of HgTe and $Hg_{0.3}Cd_{0.7}Te$ as well as superlattices (SL), which are important materials for optoelectronic devices in the far infrared, also offer this possibility at and near the L points of the BZ. They display, different from the lead chalcogenides, their narrowest band gap at Γ. HgTe is a semimetal with an inverted band structure (Γ_6 is below the Γ_8 band, opposite the situation in CdTe) at the Γ point. However, near the intersections of the BZ boundary and the [111] directions, HgTe displays the same type of band structure as CdTe with the conduction band of Λ_6 symmetry, the valence band $\Lambda_{4,5}$, and the split-off Λ_6 band with an energy difference Δ_1.[10] The E_1 gap displays a many valley behavior for excited electronic carriers. Its size is, however, markedly different for the two materials: $E_1 = 2.25$ eV for HgTe and 3.34 eV for CdTe at $T = 4.2$ K (2.90 eV for $Hg_{0.3}Cd_{0.7}Te$), with an almost linear[10] dependence on x for the intermediate concentrations of the alloy $Hg_{1-x}Cd_xTe$. At the L points the conduction bands display a minimum relative to neighboring Λ states as well as to the X ([100] directions) and K ([110] directions) critical points (electronlike effective mass), whereas the valence bands at $\Lambda_{4,5}$ show a relative maximum (holelike effective masses), at least along the BZ boundary.[10] Together with the valence band offset $[E^{VB}_{HgTe}(\Gamma_8) - E^{VB}_{CdTe}(\Gamma_8) \approx 350$ meV] in the center of the BZ (Ref. 11) the conditions for confinement of the carriers in the L valleys (in a type I quantum well) are thus well met, provided the relaxation (loss) of crystal momentum of the carriers which have been transferred to the effective-mass ellipsoids at L by resonant optical excitation is slow enough to prevent their quick return to the lower lying well at Γ. The situation is more favorable here than in the IV-IV case, since the valence band (VB) and conduction band (CB) are nearly parallel along half of the $\Gamma - L$ (Λ) line.[12,13] The gaps and offsets provide a barrier height in the CB of 0.95 eV at a $HgTe/Hg_{0.3}Cd_{0.7}Te$ interface and a barrier height of 0.26 eV for the heavy-hole VB and 0.13 eV for the light-hole VB, with an uncertainty in all values of $\pm$ 0.1 eV.[13]

We have studied the efficiency of TO, LO, and 2LO Raman scattering near the E_1 gap in HgTe epitaxial layers (EL's) and $HgTe/Hg_{0.3}Cd_{0.7}Te$ single quantum wells (SQW's) as well as multiple quantum wells (MQW's) with HgTe layer width d, where 4.8 nm $< d <$ 2000 nm. It has been verified that the optical phonon modes of HgTe and $Hg_{0.3}Cd_{0.7}Te$ do not overlap, as is well known,[10] i.e., the phonon modes are confined to the well or to the barrier, respectively, with almost vanishing amplitudes at the interfaces. Consequently, by concentrating on the Raman resonances of the HgTe well we probe the electronic states in the quantum well only. Since the E_1 conduction band states serve as intermediate states in the Raman scattering process, the Raman resonance energies display the energetic position of the band edge states subjected to confinement in the well and should be blueshifted in this case following a d^{-2} de-

TABLE I. Data of the investigated samples of $HgTe/Hg_{0.3}Cd_{0.7}Te$ quantum well structures. d (D) is the well (barrier) width in nm, $(d/D)_1$ is estimated from the growth parameters and $(d/D)_2$ is determined from from x-ray data. A single quantum well is denoted by SQW and an epitaxial layer by EL. For multiple quantum well (MQW) structures the number of periods is given.

Sample number	Orientation	Substrate	(Well/barrier) width $(d/D)_1$	$(d/D)_2$	Number of periods
Q162	(001)	$Cd_{0.96}Zn_{0.04}Te$	4/4	$4.8 \pm 0.4/-$	100
Q165	(001)	$Cd_{0.96}Zn_{0.04}Te$	6/4	7.0/3.6	100
Q148	(001)	$Cd_{0.96}Zn_{0.04}Te$	6		SQW
Q147	(001)	$Cd_{0.96}Zn_{0.04}Te$	8		SQW
Q146	(001)	$Cd_{0.96}Zn_{0.04}Te$	16		SQW
Q82	(001)	$Cd_{0.96}Zn_{0.04}Te$	16.3/6.5		120
Q65	(001)	$Cd_{0.96}Zn_{0.04}Te$	≈ 2000		EL
Q346	(110)	GaAs	5/15.5		20
Q342	(110)	CdTe	≈ 2000		EL
Q303	(111)	CdTe	12		SQW
Q343	(111)	CdTe	7.5/27	$\approx 6/21$	20

pendence, where the slope is determined by the effective mass of the carriers. In the bulk material an eightfold degeneracy occurs at L, where the gaps along opposite valleys are Kramers degenerate. This fourfold degeneracy is not lifted in HS grown along [001] or equivalent. However, it is partially raised by lowering the symmetry when growing (110) and (111) oriented HS's.[14] The new subband systems each display two resonance energies characterized by the corresponding combinations of the longitudinal and transverse effective masses due to the different intersections of the ellipsoidal valleys by the new BZ (''light'' and ''heavy'' subband system).[14,15] Special interface phonons should also exist with frequencies intermediate between the bulk TO and LO values.

Resonant Raman scattering at the L point in HS's grown in other than the (001) direction has not been studied before. We have derived selection rules for the (001), (110), and (111) orientations assuming the deformation-potential (DP) and the Fröhlich intraband (F) scattering mechanism.

A satisfactory description is obtained if the spectra of the differently oriented samples can be interpreted quantitatively using the same effective-mass tensor and the same set of relative scattering amplitudes a_{DP} and a_F. To achieve this and to eliminate wavelength dependent effects on the measured count rates due to the wavelength dependence of the detector sensitivity and the instrument transmission, the Raman intensity ratios for all samples were determined quantitatively by normalizing the spectra to a scattering standard (LO Raman line of Si, 522 cm^{-1}, at $T=1.5$ K).

The contributions of both scattering mechanisms and those of minor importance have been studied previously in detail for bulk HgTe, i.e., thick epitaxial layers, at the E_1 and $E_1+\Delta_1$ band gaps.[16] In addition, the physical background of the scattering processes has been discussed there.

II. EXPERIMENT

The experimental setup and procedure is identical to that described in Ref. 16. The $HgTe/Hg_{0.3}Cd_{0.7}Te$ samples were grown by molecular-beam epitaxy (MBE) and are nominally undoped.[17,18] In Table I the various structures under study are described. The quantum well structures and the substrates are separated by a CdTe buffer of 50 nm width. The correct orientation of the samples was controlled by Laue x-ray backscattering. It has been demonstrated recently[19] that the interfaces separating wells and barriers have an average width of three to four monolayers, which must have consequences on the position of the subband energies, leading to an increase with respect to an atomically abrupt interface, which is dependent on the well width d, especially for $d<3$ nm. An additional increase, independent of the width, is caused by a low concentration of Cd found in the well ($\approx 3-4$ %), which is due to sublimation of Cd from the hot shutter of the CdTe source when closed during growth of the HgTe well. Nonlinear diffusion could also be responsible for the low concentration of Cd in HgTe. However, a recent investigation[20] of the diffusion process based on an analysis of the optical absorption coefficient of $HgTe/Hg_{0.3}Cd_{0.7}Te$ SL as a function of the annealing time can only be explained by linear diffusion.

III. THEORY

For a quantitative interpretation of the Raman resonances at the E_1 gap in the three sample orientations under investigation, the theoretical analysis has to proceed stepwise. First the effects of different orientations of the constant energy ellipsoids with respect to the growth directions of the samples have to be studied. Next the influence of the HS's with its smaller BZ of lower symmetry than the bulk crystal on the electronic and phonon systems will be discussed. Finally, new Raman selection rules are derived, which will be compared with well known bulk results.[16]

A. Confined states at the E_1 gap in HS's

The eight ellipsoidal valleys at the L points are intersected by the new BZ along different directions and the corresponding effective masses have been derived. In Fig. 1(a) we have displayed a single constant-energy ellipsoid in the CB at the L point of the bulk with its symmetry-adapted coordinate system (x', y', z'), where z' is along the axis of rotation. Its

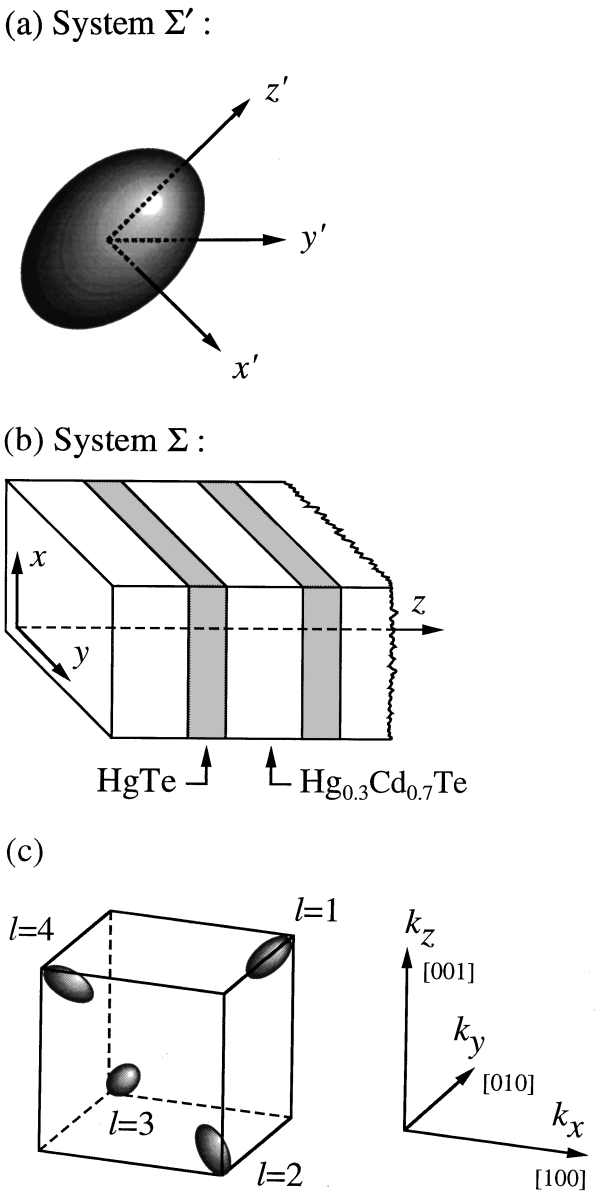

FIG. 1. Coordinate systems used in this work. (a) Primed: Symmetry-adapted system to a single constant-energy ellipsoid. (b) Unprimed: System oriented along the heterostructure growth direction z. (c) Relative orientations $\hat{\mathbf{e}}_l$ of the constant-energy ellipsoids l to the unprimed coordinate system for a (001) grown heterostructure: $\hat{\mathbf{e}}_1=3^{-1/2}(1,\ 1,\ 1)$; $\hat{\mathbf{e}}_2=3^{-1/2}(1,\ \bar{1},\ \bar{1})$; $\hat{\mathbf{e}}_3=3^{-1/2}(\bar{1},\ 1,\ \bar{1})$; $\hat{\mathbf{e}}_4=3^{-1/2}(\bar{1},\ \bar{1},\ 1)$.

long principal axis, giving the longitudinal effective mass m_l, is along z', and the transverse effective masses m_t of the bulk are $m_{x'}$ and $m_{y'}$, respectively. In the HS's of various orientations, coordinate systems have been selected with z along the actual growth directions [Fig. 1(b)]. For these coordinate systems new effective masses are derived: m_z perpendicular to the interfaces, m_x and m_y parallel to the interfaces. Whereas for a [001] grown HS all constant energy surfaces at the L points are oriented symmetrically with respect to the growth direction [Fig. 1(c)], and identical effective masses are derived (degeneracy $n_v=4$), this situation is different for the other orientations. For growth along [111] the fourfold degeneracy is raised and different masses result for the [111] gap (singlet-gap) and the triplet gaps along $[\bar{1}11]$, $[1\bar{1}1]$, and $[11\bar{1}]$. For z parallel to [110] two groups arise: [111] and $[1\bar{1}1]$, and on the other hand, $[\bar{1}11]$ and $[11\bar{1}]$. Thus for both [110] and [111] oriented growth two new subband systems with different energies will appear. These new subband systems display two Raman resonance energies for phonon scattering characterized by the various combinations of the m_t and m_l effective masses. The problem of transforming the effective-mass tensor into the various new systems has been solved by Stern and Howard[14] and we cite Table II from this work.

The confined electronic motion parallel to the growth direction z at the E_1 band gap in $HgTe/Hg_{0.3}Cd_{0.7}Te$ heterostructures can be approximately described assuming an infinite barrier height by the envelope functions $\xi^n_{\lambda,\mathbf{k}}(z)=\sqrt{2/d}\cos(n\pi z/d)$ for $n>0$, odd and $\xi^n_{\lambda,\mathbf{k}}(z)=\sqrt{2/d}\sin(n\pi z/d)$ for n even, where λ (n) is the band (subband) index. The electron motion perpendicular to the growth direction is expressed by Bloch functions containing the wave vector $\mathbf{k}$. In this approximation, the energies of the confined states are

$$E_n=\pi^2\hbar^2n^2/2m_zd^2, \tag{1}$$

with the effective masses m_z taken from Table II. Thus, in directions other than [001] two groups of energy levels are formed, the ''light'' and ''heavy'' subband systems.

Considering the transition dipole matrix elements from the electron-photon interaction operator between the HS states, the conservation of the subband index, $\Delta n=0$ (for infinite barrier height), is valid in the usual way.[21] The subband index conservation rule is relaxed if the barrier height is finite, however, the strongest transition obeys $\Delta n=0$. In addition, the intensities of Raman transitions with $\Delta n>0$ at higher energies are suppressed by an increase in the optical absorption at the E_1 edge.

The optical phonon modes in a $HgTe/Hg_{0.3}Cd_{0.7}Te$ HS's are completely confined, as already discussed. There exists no overlap between either the bulk TO and LO phonon bands of both compounds. As a consequence, the phonon-envelope functions are standing waves with the interfaces as nodal planes. Accordingly, only discrete phonon wave vectors $\mathbf{q}_p(z)=\mathbf{e}_z p\pi/d,\ p\in N$, will exist, and the phonon-envelope functions $\phi^m_{\mathbf{q}}(z)$ will have the approximate form $\phi^m_{\mathbf{q}}(z)=a^m_{\mathbf{q}}\cos(m\pi z/d)$ for $m>0$, odd and $\phi^m_{\mathbf{q}}(z)=a^m_{\mathbf{q}}\sin(m\pi z/d)$ for m even.[22] Here, $a^m_{\mathbf{q}}$ is a constant amplitude factor, and the coordinate z runs from the center of the layer to the next interface. The modes have to be grouped into odd and even modes according to the parity of the envelope function $\phi^m_{\mathbf{q}}(z)$ with respect to the center of the well or the barrier.

B. Raman selection rules at the E_1 gap in HS's

The electronic quantization at the E_1 gap in HS's modifies the Raman selection rules and resonance behavior with respect to bulk HgTe. From our experiments we have obtained the resonance enhancement of the normalized count rate C/C_{Si}, where C (C_{Si}) is the scattering rate of the sample (reference). This quantity is essentially determined[16] by the Raman scattering efficiency[23]

TABLE II. Effective masses for three HS growth directions which are derived from the principal effective masses in the corresponding ellipsoids (m_l, m_t) in the direction parallel (m_z) and perpendicular to the growth (m_x, m_y; Fig. 1). n_v is the degeneracy of each set of ellipsoids without considering Kramers degeneracy, m_c is the confinement mass derived from m_z using the approximation $m_l \gg m_t$, m_d is the approximate value for the density-of-states mass $m_d=(m_x \times m_y)^{1/2}$ for $m_l \gg m_t$ l refers to the ellipsoids in Fig. 1(c) (from Ref. 14).

Surface	m_x	m_y	m_z	m_c	n_v	m_d	l
(001)	m_t	$(m_t+2m_l)/3$	$(3m_tm_l)/(m_t+2m_l)$	$(3/2)m_t$	4	$\sqrt{(2m_tm_l)/3}$	$1 \cdots 4$
(110)	m_t	$(m_l+2m_t)/3$	$(3m_tm_l)/(m_l+2m_t)$	$3m_t$	2	$\sqrt{(m_tm_l)/3}$	1, 4
(110)	m_t	m_l	m_t	m_t	2	$\sqrt{m_tm_l}$	2, 3
(111)	m_t	m_t	m_l	m_l	1	$\sqrt{m_tm_l}$	1
(111)	m_t	$(m_t+8m_l)/9$	$(9m_tm_l)/(m_t+8m_l)$	$(9/8)m_t$	3	$\sqrt{(8m_tm_l)/9}$	2, 3, 4

$$\frac{dS}{d\Omega}=\frac{\omega_S^3\omega_L}{c^4}\frac{\hbar}{2V_cM^*\Omega_j}\frac{n_S}{n_L}|\hat{\mathbf{e}}_S^*\cdot\overleftrightarrow{R}\cdot\hat{\mathbf{e}}_L|^2[n(\Omega_j)+1]. \quad (2)$$

The scattering efficiency is dealt with as a function of the incident (scattered) photon polarization vectors $\hat{\mathbf{e}}_L$ ($\hat{\mathbf{e}}_S$) and frequencies ω_L (ω_S), the corresponding indices of refraction, n_L and n_S, the phonon frequency Ω_j of branch j, and the phonon occupation factor $n(\Omega_j)$. Here, $V_c=a_0^3/4$ is the volume and $M^*=(1/M_{\mathrm{Hg}}+1/M_{\mathrm{Te}})^{-1}$ the reduced mass of the primitive unit cell with lattice constant a_0, and c the speed of light in vacuum. $\overleftrightarrow{R}$ is the second rank Raman tensor with its nine independent components a, which comprises the predictions of Raman selection rules and relative scattering amplitudes.

For the one-phonon process, the Raman tensor $\overleftrightarrow{R}$ can be written as[24,25]

$$\begin{aligned}\overleftrightarrow{R}=&\frac{n_Ln_S}{2\pi}\frac{V_c}{u_0}\frac{1}{\hbar\omega_L}\left(\frac{e}{m_0}\right)^2A_LA_SB\sum_{\nu,\nu'}^{\mathrm{CB}}\sum_{\mu,\mu'}^{\mathrm{VB}}\delta_{\mathbf{k}_L-\mathbf{k}_S,\mathbf{q}}\\&\times\{\hat{\mathbf{e}}^j(\mathbf{q})\langle c_{\nu'}|h_{eL}|c_\nu\rangle[\langle v_{\mu'}|\mathbf{p}|c_{\nu'}\rangle\otimes\langle c_\nu|\mathbf{p}|v_\mu\rangle]\\&\times\mathcal{E}_c(\nu',\nu;\mu)\delta_{\mu,\mu'}-\hat{\mathbf{e}}^j(\mathbf{q})\langle v_\mu|h_{eL}|v_{\mu'}\rangle\\&\times[\langle v_{\mu'}|\mathbf{p}|c_{\nu'}\rangle\otimes\langle c_\nu|\mathbf{p}|v_\mu\rangle]\mathcal{E}_v(\nu;\mu',\mu)\delta_{\nu,\nu'}\}, \quad (3)\end{aligned}$$

where $u_0=(\hbar V_c/2VM^*\Omega_j)^{1/2}$ is the zero-point amplitude of the optical phonon, which contains the scattering volume V. In Eq. (3), $A_{L(S)}=(\hbar/2n_{L(S)}^2\omega_{L(S)}V\varepsilon_0)^{1/2}$ is a prefactor due to the quantization of the vector potential, where ε_0 is the vacuum permittivity, and $\mathbf{k}_L$ ($\mathbf{k}_S$) denotes the wave vector of the incident (scattered) photon. The momentum operator $\mathbf{p}$ enters Eq. (3) via the absorption and emission terms of the electron-photon interaction, whereas the matrix elements of h_{eL} describe the electron-phonon coupling.

The two electron-phonon scattering mechanisms which obviously provide the essential part of the observed Raman intensities in our samples[16] are the dipole-allowed scattering by TO and LO phonons, which arises from the DP interaction, and dipole-forbidden scattering by LO phonons due to F coupling. There exists no evidence in our experiments that other possible processes, such as the impurity-induced scattering mechanism (see, e.g., Ref. 26), play an appreciable role.[16]

For DP scattering, h_{eL} is given by $\mathbf{V}_{\mathrm{DP}}^j(\mathbf{r}')=[\partial V_{\mathrm{eff}}/\partial\mathbf{u}^j(\mathbf{r}')]a_0$,[27] which expresses the change in the electron effective potential V_{eff} induced by the phonon perturbation $\mathbf{u}^j(\mathbf{r}')$ corresponding to the branch j, whereas in the case of F interaction $h_{eL}=\hat{\mathbf{q}}$. For Raman scattering at the E_1 gap in a HS the prefactor B has the form[22,28]

$$B=\begin{cases}\left(\dfrac{u_0}{a_0}\right)\dfrac{1}{\sqrt{N_{\mathrm{DP}}}}\displaystyle\int_d dz\ \xi_{\lambda,\mathbf{k}}^{n*}(z)\left[-\frac{\partial\phi_{\mathbf{q}}^m(z)}{\partial z}\right]\xi_{\lambda',\mathbf{k}+\mathbf{q}}^{n'}(z)\,\delta_{n,n'} & \text{for DP interaction,}\\ \left(\dfrac{-iC_F}{q\sqrt{V}}\right)\dfrac{1}{\sqrt{N_F}}\displaystyle\int_d dz\ \xi_{\lambda,\mathbf{k}}^{n*}(z)[\phi_{\mathbf{q}}^m(z)]\xi_{\lambda',\mathbf{k}+\mathbf{q}}^{n'}(z)\,\delta_{n,n'} & \text{for } F \text{ interaction,}\end{cases} \quad (4)$$

where $\delta_{n,n'}$ takes care of the conservation of the subband indices ($n=n'$), C_F is the Fröhlich coupling constant,[23] and N_{DP} and N_F are normalization constants suitably selected. In the case of DP interaction, the parity of $\partial\phi_{\mathbf{q}}^m(z)/\partial z$ must be even (for $\Delta n=0$) for the integral in Eq. (4) to be finite, i.e., $\phi_{\mathbf{q}}^m(z)$ must be odd. For the F coupling, a finite value of this integral requires that $\phi_{\mathbf{q}}^m(z)$ has to be even. The evaluation of the integrals in Eq. (4) shows that their contributions decrease strongly with increasing m.[29] Accordingly, it is sufficient to consider only the lowest-order contributions of $m=1,2$.

In Eq. (3), $\hat{\mathbf{e}}^j(\mathbf{q})$ denotes the unit vector of the relative sublattice displacement $\mathbf{u}^j(\mathbf{r}')$, which is parallel (perpendicular) to the wave vector $\mathbf{q}$ for LO (TO) phonons. The summations extend over the conduction subbands CB and the valence subbands VB, the c and v states are indexed by ν, ν', μ, and μ'. The resonance denominators $\mathcal{E}_c$ and $\mathcal{E}_v$ are given by

$$\mathcal{E}_c(\nu',\nu;\mu):=\sum_{\mathbf{k}}\frac{1}{[E_{\nu'}(\mathbf{k}-\mathbf{q})-E_{\mu}(\mathbf{k}-\mathbf{k}_L)-\hbar\omega_S][E_{\nu}(\mathbf{k})-E_{\mu}(\mathbf{k}-\mathbf{k}_L)-\hbar\omega_L]},$$

$$\mathcal{E}_v(\nu;\mu',\mu):=\sum_{\mathbf{k}}\frac{1}{[E_{\nu}(\mathbf{k})-E_{\mu'}(\mathbf{k}-\mathbf{k}_S)-\hbar\omega_S][E_{\nu}(\mathbf{k})-E_{\mu}(\mathbf{k}-\mathbf{k}_L)-\hbar\omega_L]}, \tag{5}$$

where $E_{\nu(\nu')}$ and $E_{\mu(\mu')}$ are subband energies of the conduction and valence states, respectively, involved in the matrix elements of the operators h_{eL} and $\mathbf{p}$ occurring in Eq. (3). A comprehensive review of the evaluation of Raman tensors at the E_1 gap in semiconductors has been given by Richter *et al.*[30] The general problem of Raman scattering by optical phonons in HS's has been treated in detail by Huang *et al.*[22]

The Raman tensor $\overleftrightarrow{R}_{\mathrm{DP}}$ of DP scattering can be calculated from Eqs. (3)–(5). Its diagonal elements, taken between the states of Λ_6 and $\Lambda_{4,5}$ symmetry in the CB and the VB, respectively, are the two-band terms, the off-diagonal elements are due to phonon mediated mixing of the valence bands (three-band terms). In the following we restrict ourselves to an evaluation of the two-band processes, which provide the essential part to the allowed Raman transition amplitude in the vicinity of the E_1 gap of HgTe.[16] The contributions of the eight valleys have to be added coherently only for the n_ν degenerate gaps (Σ_l) including the spin degeneracy:

$$\overleftrightarrow{R}_{\mathrm{DP}}=-\frac{\sqrt{3}f}{64\pi}\frac{1}{4\pi\varepsilon_0}\left(\frac{e}{m_0}\right)^2\frac{a_0^2}{a^{*3}}\frac{1}{\omega_L(\omega_L\omega_S)^{1/2}}\frac{1}{(\hbar\Omega_j^m)^2}$$

$$\times P'^2 d_{1,o}^5(\ln\beta-\ln\alpha)2\sum_l \hat{\mathbf{e}}^j(\mathbf{q})\cdot\hat{\mathbf{e}}_l\overleftrightarrow{T}_l, \tag{6a}$$

$$\alpha:=\frac{\hbar\omega_L-E_1^{n,n'}}{\hbar\Omega_j^m},\quad \beta:=\alpha-1. \tag{6b}$$

Here, $d_{1,o}^5=d_{1,o}^5(c)-d_{1,o}^5(v)$, where the optical deformation potential $d_{1,o}^5(c)$ $[d_{1,o}^5(v)]$ describes the phonon-induced modulation of the CB (VB) at the E_1 band gap.[27,31] In Eq. (6a), we have defined $a^*:=(\hbar/2\mu_\perp\Omega_j^m)^{1/2}$, where $\mu_\perp$ is the reduced effective mass of the electron-hole pair at the E_1 gap, and f is the fraction of the Λ line in the BZ where the CB and the VB are nearly parallel [$f\approx 1/2$ in HgTe (Ref. 12)]. The transition energy at E_1 between the subband states n and n' in the VB and the CB, respectively, is denoted by $E_1^{n,n'}$, whereas the mth confined phonon frequency of branch j is indicated by Ω_j^m. Furthermore, $P':=i\langle X'|p_{x'}|S\rangle=i\langle Y'|p_{y'}|S\rangle$ is the Kane matrix element,[32,33] and the $\overleftrightarrow{T}_l$ matrices, which are projection operators $1-|\hat{\mathbf{e}}_\mathbf{l}\rangle\langle\hat{\mathbf{e}}_l|$ onto the $l=1$, 2, 3, 4 valleys [Fig. 1(c)], where the $\hat{\mathbf{e}}_l$ vectors are unit vectors pointing in the direction of the lth valley, are taken from the Appendix. The selection rules for DP scattering are determined by the sum in Eq. (6a), where the unit vectors $\hat{\mathbf{e}}^j(\mathbf{q})$ and $\hat{\mathbf{e}}_l$ have to be evaluated within the unprimed coordinate system of the sample [Figs. 1(b) and (c)]. Final results for the three surface orientations under study have been summarized in Table III.

The Raman tensor $\overleftrightarrow{R}_F$ of F scattering at the E_1 gap in a HS can be written as

$$\overleftrightarrow{R}_F=-i\frac{I(z)}{16\pi^2}\frac{1}{4\pi\varepsilon_0}\left(\frac{e}{m_0}\right)^2\frac{a_0^2}{V^{1/2}u_0}\frac{1}{\omega_L(\omega_L\omega_S)k^{1/2}}\frac{1}{(\hbar\Omega_{\mathrm{LO}}^m)^2}$$

$$\times P'^2 C_F(\ln\beta-\ln\alpha)\Delta M\hat{\mathbf{e}}^{\mathrm{LO}}(\mathbf{q})\cdot\mathbf{q}_z 2\sum_l \overleftrightarrow{T}_l, \tag{7a}$$

where

$$\Delta M:=\frac{\partial^2}{\partial q_z^2}\{[M(q_z)]_{n'}-[M(q_z)]_n\}_{q_z=0}, \tag{7b}$$

and

$$[M(q_z)]_n:=\int_d dz\ \xi_{\lambda,\mathbf{k}}^{n*}(z)\exp(iq_z z)\xi_{\lambda,\mathbf{k}}^{n}(z). \tag{7c}$$

In Eqs. (7a)–(7c), $q_z=m\pi/d$ and $I(z):=\int d(a^*k_z)$. Equation (7) indicates that in a HS the F scattering may be dipole forbidden if the envelope functions for the electrons and holes are identical, which is, however, not generally obeyed.[34] The resulting selection rules from the summations over the n_ν degenerate gaps in the different growth directions are comprised in Table III.

We summarize the influence of the interfaces in a HS on resonant Raman scattering at the E_1 gaps as follows: The electron-phonon interaction results in $\Delta n=0$ Raman transitions, but contributions with $\Delta n=2$, 4 will also occur with their intensity decreasing with increasing n. Odd phonon-envelope modes will be activated by DP interaction with the largest contribution for $m=1$, whereas even modes are excited by F scattering, $m=2$ being the largest. The calculated scattering amplitudes differ by certain factors from the bulk case, but most conspicuously the Raman selection rules will be governed by raising the fourfold degeneracy of the E_1 gaps for growth directions other than [001] (Table II). The three growth directions demonstrate different energy separations between the subbands. The calculated differences for the Raman intensities between the various directions are quite conspicuous in some cases as shown in Table III.

We shall discuss only a few, albeit characteristic differences for the various growth directions: No changes occur for heterostructures grown in the [001] direction except for frequency shifts due to quantum confinement (see below) and a possible change in the amplitudes a_F and $a_{\mathrm{TO(LO)}}$ by a reduction of the symmetry (cubic to tetragonal). However, in the [110] direction, two pairs of degenerate valleys ($l=1,4$) and ($l=2,3$) exhibit quite different Raman intensities in polarized [$\overline{z(x,x)z}$ or $\overline{z(y,y)z}$] and in depolarized

TABLE III. Raman selection rules of deformation potential (DP) and Fröhlich intraband (F) backscattering from (001), (110), and (111) surfaces of zinc-blende crystals in the vicinity of the E_1 gap. The values for heterostructures are compiled here together with previous bulk results (Ref. 16). a_F is the LO scattering amplitude due to the F mechanism, $a_{\mathrm{LO(TO)}}$ is the LO (TO) scattering amplitude due to the DP mechanism. a_F, a_{LO}, and a_{TO} are not specified in this work, the values in the bulk differ from the amplitudes in a HS.

(001) face: $x=[100]$, $y=[010]$, $z=[001]$, $x_1=\frac{1}{\sqrt{2}}[110]$, $y_1=\frac{1}{\sqrt{2}}[\bar{1}10]$
All gaps degenerate in heterostructures

	Selection rules	
Scattering geometry	Bulk	Heterostructure
$\overline{z(}x,x)z$, $\overline{z(}y,y)z$	$\lvert a_F\rvert^2$	$\lvert a_F\rvert^2$
$\overline{z(}y,x)z$, $\overline{z(}x,y)z$	$\lvert a_{\mathrm{LO}}\rvert^2$	$\lvert a_{\mathrm{LO}}\rvert^2$
$\overline{z(}x_1,x_1)z$	$\lvert a_F+a_{\mathrm{LO}}\rvert^2$	$\lvert a_F+a_{\mathrm{LO}}\rvert^2$
$\overline{z(}y_1,y_1)z$	$\lvert a_F-a_{\mathrm{LO}}\rvert^2$	$\lvert a_F-a_{\mathrm{LO}}\rvert^2$

(110) face: $x=\frac{1}{\sqrt{2}}[\bar{1}10]$, $y=[001]$, $z=\frac{1}{\sqrt{2}}[110]$
''Heavy'' gaps $l=1,4$ and ''light'' gaps $l=2,3$ in heterostructures

	Selection rules		
Scattering geometry	Bulk		Heterostructure
$\overline{z(}x,x)z$	$\frac{9}{16}\lvert a_F\rvert^2+\lvert a_{\mathrm{TO}_y}\rvert^2$	$l=1,4$:	$\frac{9}{64}\lvert a_F\rvert^2+\frac{9}{4}\lvert a_{\mathrm{TO}_y}\rvert^2$
		$l=2,3$:	$\frac{9}{64}\lvert a_F\rvert^2+\frac{1}{4}\lvert a_{\mathrm{TO}_y}\rvert^2$
$\overline{z(}y,y)z$	$\lvert a_F\rvert^2$	$l=1,4$:	$\frac{1}{16}\lvert a_F\rvert^2+\lvert a_{\mathrm{TO}_y}\rvert^2$
		$l=2,3$:	$\frac{9}{16}\lvert a_F\rvert^2+\lvert a_{\mathrm{TO}_y}\rvert^2$
$\overline{z(}y,x)z$, $\overline{z(}x,y)z$	$\lvert a_{\mathrm{TO}_x}\rvert^2$	$l=1,4$:	0
		$l=2,3$:	$\lvert a_{\mathrm{TO}_x}\rvert^2$

(111) face: $x=\frac{1}{\sqrt{6}}[11\bar{2}]$, $y=\frac{1}{\sqrt{2}}[\bar{1}10]$, $z=\frac{1}{\sqrt{3}}[111]$
''Heavy'' gap $l=1$ and ''light'' gaps $l=2,3,4$ in heterostructures

	Selection rules		
Scattering geometry	Bulk		Heterostructure
$\overline{z(}x,x)z$, $\overline{z(}y,y)z$	$\left\lvert\frac{5}{6}a_F-\frac{1}{\sqrt{3}}a_{\mathrm{LO}}\right\rvert^2+\frac{2}{3}\lvert a_{\mathrm{TO}_x}\rvert^2$	$l=1$:	$\frac{27}{16}\lvert a_{\mathrm{LO}}\rvert^2$
		$l=2,3,4$:	$\left\lvert\frac{5}{6}a_F+\frac{5}{4\sqrt{3}}a_{\mathrm{LO}}\right\rvert^2+\frac{2}{3}\lvert a_{TO_x}\rvert^2$
$\overline{z(}y,x)z$, $\overline{z(}x,y)z$	$\frac{2}{3}\lvert a_{\mathrm{TO}_y}\rvert^2$	$l=1$:	0
		$l=2,3,4$:	$\frac{2}{3}\lvert a_{\mathrm{TO}_y}\rvert^2$

$[\overline{z(}x,y)z$ or $\overline{z(}y,x)z]$ spectra. The contributions of the four valleys to the spectra derived from the light and heavy masses are pronouncedly different. As an example, the DP scattering in the depolarized spectra is concentrated only in the spectra of the light mass, because the $l=1,4$ (heavy mass) gaps do not provide projections of the transition dipole moments in the directions considered here. In the same manner the dipole-forbidden F scattering is distributed with different weights over the two pairs of gaps. In the case of the [111] direction, F scattering occurs solely in the triply degenerate gaps ($l=2$, 3, 4). On the other hand, TO scattering is not influenced by the presence of HS interfaces in this case.

IV. EXPERIMENTAL RESULTS

A. Samples grown in (001) direction

A typical Raman spectrum of a (001) grown $HgTe/Hg_{0.3}Cd_{0.7}Te$ HS in the spectral range of the LO and 2LO phonon scattering is shown in Fig. 2. Near 118 cm^{-1}

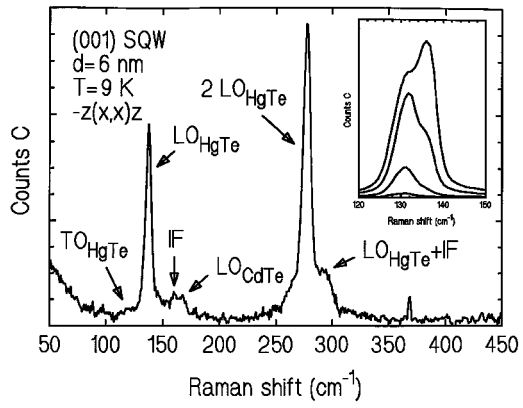

FIG. 2. Raman spectrum of a $HgTe/Hg_{0.3}Cd_{0.7}Te$ SQW (001), sample Q148 (Table I), close to resonance with the E_1 gap (laser energy: 18 106 cm^{-1}). The inset displays the fine structure in the range around the HgTe-like LO phonon of the similar sample Q82, where the total scattering intensity increases with the laser frequency, i.e., the resonance of the 131 cm^{-1} mode occurs at lower energy.

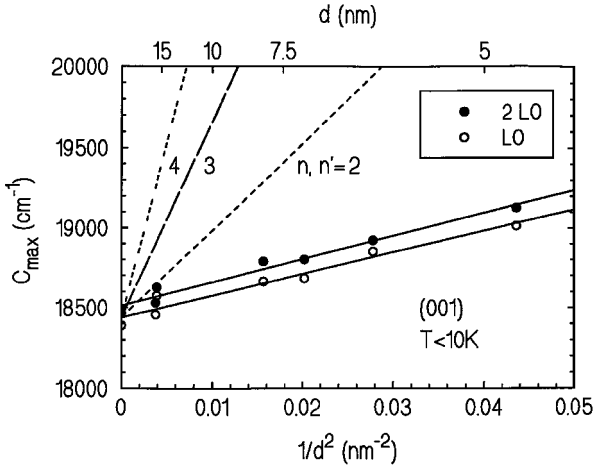

FIG. 3. Quantum confinement effects of several SQW's and MQW's of varying well width d grown in the (001) direction (see Table I). The effective gap energies (laser energies of maximum Raman scattering intensities C_{max}) are plotted against d^{-2} [Eq. (1)]. The subband energies of second and higher orders n, n' have been calculated using the effective masses derived from the $n,n'=1$ results.

the TO_{HgTe} is found as a weak shoulder, which should not occur in this geometry according to the selection rules (Table III). Its appearance is either due to a nonideal backscattering geometry (finite angle of incidence) or due to the presence of crystal defects. However, the low intensity of this ''forbidden'' mode indicates the good quality of the samples used and the correct optical alignment of the experimental setup. At 136 cm^{-1} the LO phonon of HgTe is observed, the 2LO process at 274 cm^{-1} has comparable intensity near resonance and is a further indication for the good quality of the MBE samples,[35] because at high defect concentrations the intensity of the LO process increases with respect to higher-order LO lines due to a relaxation of the wave vector conservation for the 1LO scattering process.[16]

In contrast to the bulk material[16] we observe two other modes below 200 cm^{-1} (IF at 158 cm^{-1} and LO_{CdTe} at 165 cm^{-1}). The CdTe-like LO mode is very weak and rarely exceeds the noise level. No resonance behavior is displayed in the energy region of the laser used for our experiments because the E_1 gap in the $Hg_{0.3}Cd_{0.7}Te$ alloy has a different energy. The IF mode can be interpreted as due to an interface mode. Interface (IF) modes with this wave number are to be expected.[36,37] It displays a weak Raman resonance, similar to the LO_{HgTe} mode, because it couples to the LO phonons in the well. Another weak Raman signal (LO+IF) could be detected at 295 cm^{-1}, whose energy equals the sum of the LO and IF phonon frequencies. Consequently, this excitation can be attributed to a second-order process in which the electron-hole pair is scattered twice, once by an LO phonon and once by an IF phonon.

The inset in Fig. 2 demonstrates the existence of two mode components between 130 cm^{-1} and 140 cm^{-1}. In addition to the signal at 136 cm^{-1} (LO_{HgTe}), there exists a peak at 131 cm^{-1}, whose relative intensity depends on the frequency of the incident laser. This fact was thought to be due to a surplus flux of Hg during the growth process, producing Te-3Hg-Cd clusters.[38] However, our investigations, especially the observation of the 131 cm^{-1} mode in nominally pure epitaxial HgTe layers, support the results of a lattice dynamical calculation of Talwar and Vandevyver[39] that a Te ion on a Hg site (Te antisite) gives rise to a local mode of the correct frequency 131 cm^{-1}.

The general appearance of the Raman resonance profile of a HgTe epitaxial layer at the E_1 gap has been published previously.[16] In order to examine confinement effects on the electronic states at the E_1 gap in heterostructures, the Raman resonance enhancement of the LO_{HgTe} and the $2LO_{HgTe}$ phonon scattering has been investigated for an epitaxial layer as well as quantum wells with different well widths d. The laser energies displaying the maximum scattering cross section for LO and 2LO processes are plotted as a function of $1/d^2$ in Fig. 3. A definite blueshift for decreasing well widths is clearly observed, resulting in a linear dependence on $1/d^2$.

The confinement masses m_c have been derived from the slopes of the solid lines in Fig. 4 assuming infinitely high barriers. We have obtained $m_c=0.209m_0$ from the LO resonance and $m_c=0.233m_0$ for the 2LO resonance. Taking the relationship between m_c and the transverse mass m_t given in Table II into account ($m_c \approx 3/2m_t$), an experimental value for the transverse mass m_t at the E_1 gap is obtained: $m_t=0.14m_0$ (from LO) and $m_t=0.15m_0$ (from 2LO). Effective masses from $\mathbf{k}\cdot\mathbf{p}$ theory have been derived in conjunction with reflection measurements at HgTe epilayers: $m_t^{CB}=0.09m_0$ and $m_t^{lh}=0.219m_0$, resulting in $m_t^{\mathbf{k}\cdot\mathbf{p}}=(1/m_t^{CB}+1/m_t^{lh})^{-1}=0.07m_0$.[16] Other values for the effective masses at E_1 have been obtained from tight-binding calculations[15,40] resulting in $m_t^{tb}=0.22m_0$. Our experimental value m_t^{exp} is thus intermediate between the two calculated results,

$$m_t^{\mathbf{k}\cdot\mathbf{p}} < m_t^{exp} < m_t^{tb},$$

which is very satisfying. The results presented in Fig. 3 indicate the existence of confined charge carriers with crystal momenta near the L points of the BZ, localized in the HgTe wells (type I HS). This is clear evidence for confinement in

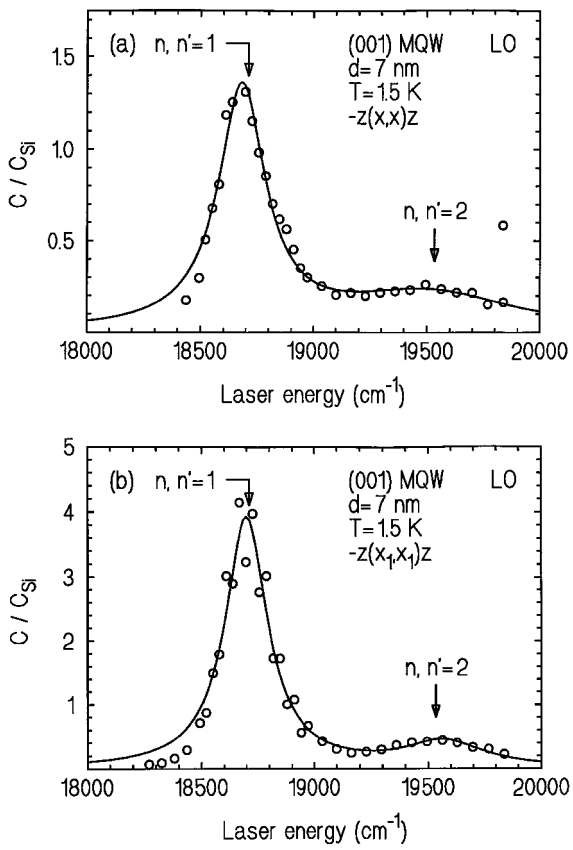

FIG. 4. Raman resonances of the LO phonon scattering in the MQW Q165 (Table I) for two different geometries defined in Table III. The experimental count rates C have been normalized with respect to a Si standard (C_{Si}). The arrows indicate the positions of the calculated interband transitions using the observed effective masses and the well widths determined by x-ray scattering. The solid lines are drawn to serve as a guide to the eye.

Hg based II-VI materials outside Γ and at energies above the lowest gap. Tejedor *et al.*[41] have previously presented evidence for a similar confinement in the III-V material GaSb-AlSb [(001) SL] at L by observing the Raman resonance at the E_1 edge.

Using the average effective mass $m_t^{\mathrm{exp}} \approx 0.145 m_0$ as determined above, the energies of higher subband transitions ($n=2 \rightarrow n'=2$) can be easily determined from Eq. (1) and compared with the Raman resonance above the lowest subband transition (Fig. 4). A weak resonance which peaks within 50 cm^{-1} of the calculated position has been observed both in $\overline{z(x,x)}z$ and in $\overline{z(x_1,x_1)}z$ geometry (Table III). Thus the existence of this secondary maximum has been verified.

B. Samples grown in [110] and [111] directions

Taking the effective mass m_t^{exp} for the [001] direction and assuming $m_l \gg m_t$, the effective gaps for the [110] and [111] grown samples have been plotted in Fig. 5 as a function $1/d^2$ using the data from Table II. Splitting of the gap energies in directions other than [001] becomes evident. The energies from this plot have been used in the following figures to indicate the calculated positions of the ''light'' and ''heavy'' resonances with arrows.

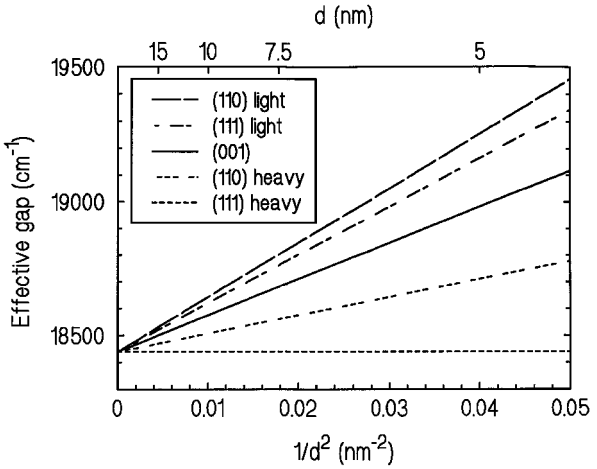

FIG. 5. Calculated effective gap energies for (001), (110), and (111) grown samples as a function of the well width d. The calculations are based on the experimental value of $m_t^{\mathrm{exp}}=0.145 m_0$ and on the ''light'' and ''heavy'' effective masses of Table II, $m_l \gg m_t$ has been assumed.

In Fig. 6 the $\overline{z(x,x)}z$ Raman resonances for a (110) sample with well width $d=5$ nm, and a (111) sample with $d=12$ nm, have been compiled for the LO and the TO phonon scattering. The predicted splitting into two resonances is clearly obvious for the TO phonon in the (110) sample [Fig. 6(a)] but could not be resolved in the (111) sample with the larger well width [Fig. 6(b)]. The calculated confinement effects as displayed in Fig. 5 predict the experimental results, i.e., position of maxima and size of splitting, very well. The intensity relationship between the light and heavy resonances for LO and TO phonons as predicted by the selection rules in Table III is also met, at least qualitatively. It can be concluded that the F mechanism, whose Raman intensity is of equal strength for both resonances, is responsible for LO scattering in (110). The scattering amplitude of the TO phonon is three times stronger for the heavy resonance than for the light one, in fair agreement with theory. The lower intensity of the light LO resonance as compared to the heavy one is, at least partially, due to an increase of absorption above the heavy E_1 energy gap. Absorption corrections, which are proportional to the density-of-states masses (Table II), have not been performed, nor have the envelope functions, which determine the transition matrix elements $[M(q_z)]_n$ [Eq. (7)], been calculated and considered. Consequently, the scattering amplitudes a_F, a_{LO}, and a_{TO} (Table III) are different from their bulk values in a HS. These differences have not been calculated here.

In Fig. 7 the LO and TO resonances of a (110) bulk sample are shown in parallel and crossed polarizations, together with the $\overline{z(y,x)}z$ resonance for the MQW of Fig. 6(a). In the $\overline{z(y,x)}z$ geometry only the TO phonon is active both in the bulk and in the HS, as predicted in Table III and in Ref. 16. The TO resonances in the bulk peak near 18 350 cm^{-1}, the difference of about 100 cm^{-1} between $\overline{z(x,x)}z$, and $\overline{z(y,x)}z$ geometry has been discussed in Ref. 16 but has not yet been satisfactorily interpreted. A comparison of Fig. 7(a) with Fig. 6(a), and Fig. 7(b) with Fig. 7(c) clearly demonstrates the existence of confinement effects at the E_1 gap. Between the bulk and a quantum well with $d=5$ nm there

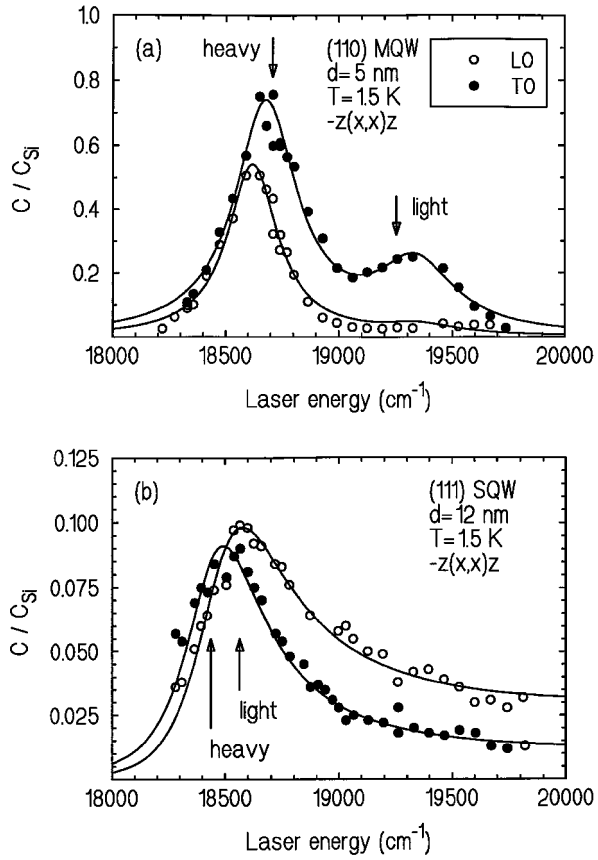

FIG. 6. Confinement effects in a (110) sample [(a), Q346] and a (111) sample [(b), Q303] for the LO and TO modes. The arrows indicate the calculated resonance energies taken from Fig. 5.

exists a frequency shift of more than 1000 cm^{-1} for the TO resonance in $\overline{z(y,x)}z$ geometry, which is the combined result of light-heavy mass splitting and confinement. The frequency shift is larger than expected for a 5 nm well width as shown in Fig. 5. This is most probably due to the fact that, for low d and an interface width of about four monolayers, the shape of the potential well is roughly parabolic rather than rectangular as assumed in the calculation of Fig. 5, with a larger effective band gap for the parabolic case.

Figure 8 together with Fig. 6(b) shows effects of both confinement and selection rules (Table III) for the two (111) grown samples. The arrows again indicate the calculated positions (Fig. 5) of the resonances, in Fig. 8(a) for the $d=12$ nm sample, in Fig. 8(b) and Fig. 8(c) for the $d\approx 6$ nm sample. For the latter, as for Fig. 7, we have to assume a nonrectangular well shape, corresponding to a square well of $d\approx 4.5$ nm. As expected (Table III), only TO phonons are active at the light gap in crossed polarization, whereas LO phonons are more intense than TO in the parallel geometry, in agreement with the selection rules. Both the DP and F mechanisms contribute to the intensity. The observed resonances are rather asymmetric [Fig. 8(b)], perhaps due to unusually strong fluctuations of the well width.

Finally, Fig. 9 displays resonances observed for second-order Raman processes (LO+IF and 2LO). The frequency shift between polarized and depolarized scattering (light and heavy gap) corresponds to the value found in Fig. 7, the

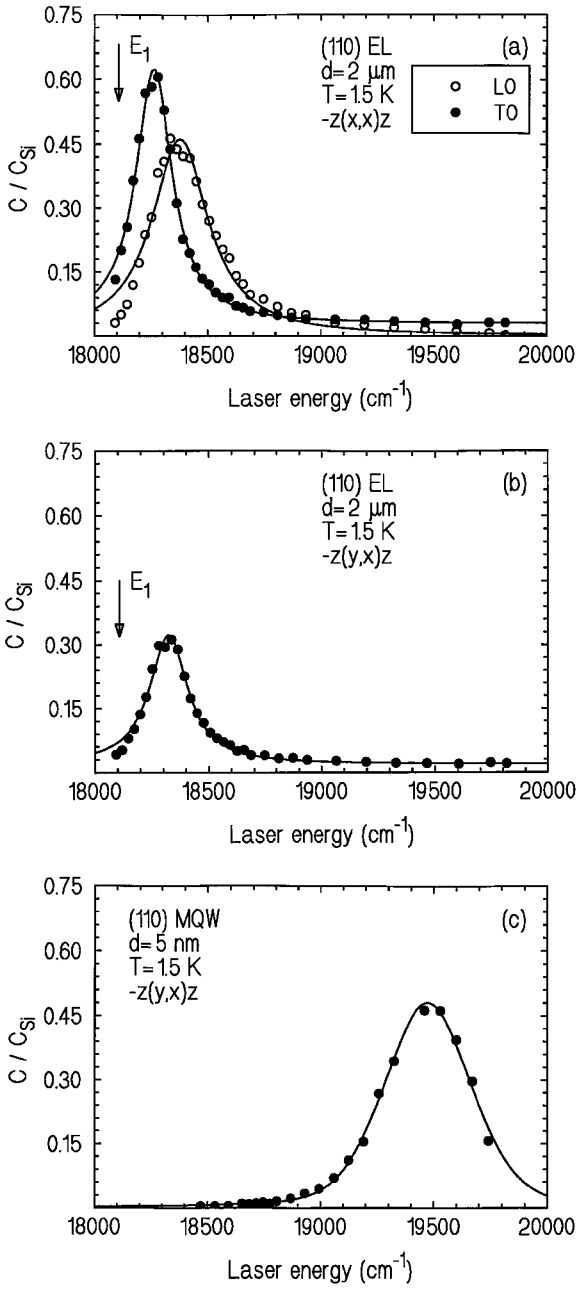

FIG. 7. Comparison of Raman resonances for TO and LO scattering in (110) grown samples in an EL [Q342, (a) and (b)] and in a MQW [Q346, (c)]. The arrows in (a) and (b) indicate the E_1 transition energies as obtained from a reflectivity study (Ref. 16). The frequency difference between the maxima in (a) and 6(a), and in (b) and (c), are the result of quantum confinement of the heavy or light mass, respectively, at the E_1 gap.

stronger intensity observed for the polarized geometry indicates that the Fröhlich mechanism is most effective for the 2LO scattering.

V. CONCLUSIONS

We have performed resonant Raman scattering experiments in epitaxially grown $HgTe/Hg_{0.3}Cd_{0.7}Te$ heterostructures. Using laser energies in the range of the E_1 gap of HgTe, we have observed Raman signals from LO and TO

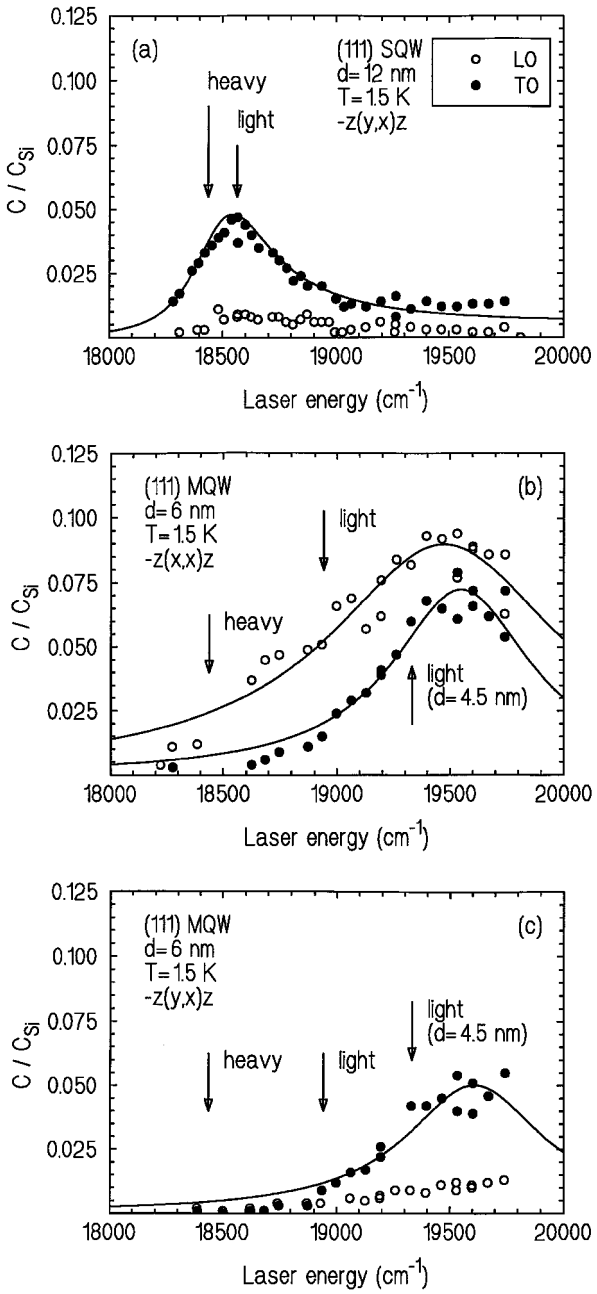

FIG. 8. Raman resonances in (111) grown samples Q303 (a) and Q343 (b,c) for LO and TO excitations. As was the case previously, the arrows indicate the calculated resonance positions. The additional arrows in (b) and (c) mark the calculated light gap energies under the assumption of an effective well width of $d=4.5$ nm due to a nonrectangular well shape.

phonons within the wells with the frequencies of bulk HgTe (TO: 118 cm^{-1}, LO: 136 cm^{-1}). These modes are heavily damped in the $Hg_{0.3}Cd_{0.7}Te$ barriers (''confined'' modes). Thus their resonance behavior permits the investigation of the electronic states within the HgTe wells. In addition to the LO and TO modes, two other phononlike modes are observed in the spectra. One can be interpreted as an interface mode, whereas the other excitation (local mode at 131 cm^{-1}) probably has its origin in a substitutional defect (Te on a Hg site).[39]

A plot of the LO and 2LO resonances as a function of the

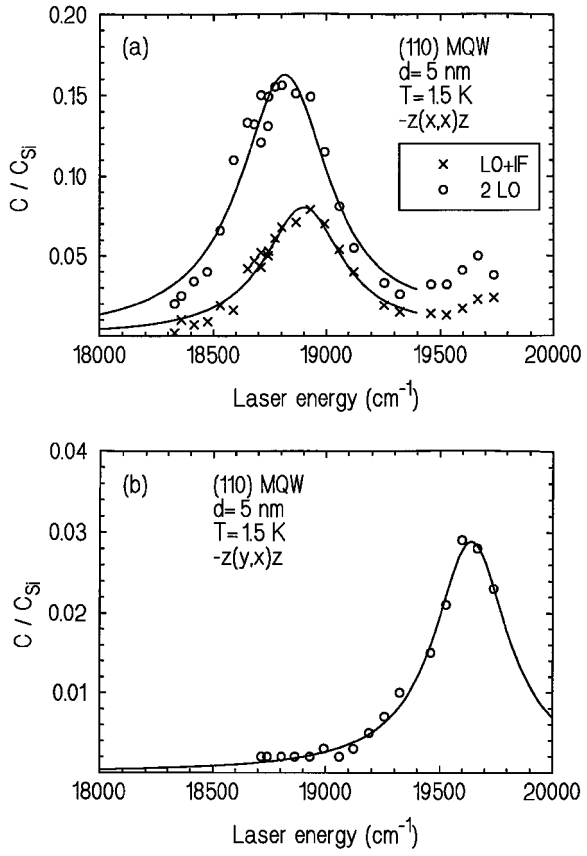

FIG. 9. Higher-order Raman resonances (2LO and LO+IF) in the (110) sample Q346, for (a) polarized $[\overline{z(x,x)z}]$ and (b) depolarized $[\overline{z(y,x)z}]$ geometry.

inverse square of the well width d (4.8 nm $\leqslant d \leqslant$ 2000 nm) is linear (Fig. 3), as expected for a quantum well with a large potential drop in a HS of type I. This is direct proof of the confinement of carriers at the E_1 gap, i.e., near the L points of the BZ. The transverse effective mass m_t is found to be $m_t=0.145m_0$, and the assumption that $m_l \gg m_t$ was confirmed by the good agreement with experiment. This result is supported by our observations using (110) and (111) grown samples. The (001) values are found to lie intermediate between those calculated with $\mathbf{k}\cdot\mathbf{p}$ and tight-binding models. Our model correctly describes the observation of a Raman resonance with an excited subband. Differences between epilayers and multiple quantum wells have not been found, which indicates that the envelope functions of the electronic states are localized just as the phonons in the wells and are heavily damped in the $Hg_{0.3}Cd_{0.7}Te$ barriers.

The degeneracy of the E_1 gap is lifted for (110) and (111) grown samples due to a lowering of symmetry. Two clearly separate resonance maxima occur. Their positions can be well predicted theoretically using the effective masses given above. The Raman selection rules are completely different for these orientations as compared to the bulk. They are calculated here for the E_1 gap in the HS using the well established models for deformation potential and Fröhlich intraband scattering. There is at least a qualitative agreement between the calculated results and the experimental data. For a quantitative comparison, values for the optical absorption in the HS as well as the analytical form of the envelope

functions are needed to calculate the transition matrix elements $M(q_z)_n$. Such calculations are highly desirable.

The existence of quantum confinement effects at the E_1 gap, i.e., above the E_0 gap, is based on the observations of energy shifts of the electronic subbands, which are linear in d^{-2}, and on the correct predictions of the energy gaps corresponding to light and heavy masses in growth directions of lower symmetry. Is there a chance that these effects are feigned by a small residual concentration of Cd in the wells, which increases slightly with decreasing d due to nonlinear diffusion? An additional Cd concentration of about 4% in the narrowest well would be required to fit the data. We think that this question can be negated for the following reasons: No experimental evidence of nonlinear diffusion exists for our samples.[20] They did not experience an annealing treatment which is found necessary to produce this effect.[19,42] Since nonlinear diffusion is presumably mediated by defects such as vacancies or interstitials,[19] such effects should be more effective in layers grown in [110] and [111] directions with higher defect concentrations due to the larger lattice mismatch with the substrate. As has been shown above, the results on quantum confinement obtained in these samples agree however very well with the calculated results using effective masses obtained from high quality (001) samples with low defect concentration. The observed linear dependence of the energy shift on d^{-2} is clearly indicative of quantum confinement but difficult to be interpreted by nonlinear diffusion.

ACKNOWLEDGMENTS

The authors are grateful to S. Einfeldt, Y. S. Wu, and L. Chang for growing the samples used and to E. Bangert, J. Kraus, and V. Latussek for valuable discussions. The Deutsche Forschungsgemeinschaft and the Bundesministerium für Bildung, Wissenschaft, Forschung und Technologie have supported this investigation.

APPENDIX

The $\overleftrightarrow{T}_l$ matrices for the growth directions defined in Table III read

[100] orientation:[43]

$$\overleftrightarrow{T}_1=\frac{1}{6}\begin{pmatrix} 2 & -1 & -1 \\ -1 & 2 & -1 \\ -1 & -1 & 2 \end{pmatrix}, \quad \overleftrightarrow{T}_2=\frac{1}{6}\begin{pmatrix} 2 & 1 & 1 \\ 1 & 2 & -1 \\ 1 & -1 & 2 \end{pmatrix}, \tag{A1}$$

$$\overleftrightarrow{T}_3=\frac{1}{6}\begin{pmatrix} 2 & 1 & -1 \\ 1 & 2 & 1 \\ -1 & 1 & 2 \end{pmatrix}, \quad \overleftrightarrow{T}_4=\frac{1}{6}\begin{pmatrix} 2 & -1 & 1 \\ -1 & 2 & 1 \\ 1 & 1 & 2 \end{pmatrix};$$

[110] orientation:

$$\overleftrightarrow{T}_{1,4}=\frac{1}{6}\begin{pmatrix} 3 & 0 & 0 \\ 0 & 2 & \mp\sqrt{2} \\ 0 & \mp\sqrt{2} & 1 \end{pmatrix}, \tag{A2}$$

$$\overleftrightarrow{T}_{2,3}=\frac{1}{6}\begin{pmatrix} 1 & \mp\sqrt{2} & 0 \\ \mp\sqrt{2} & 2 & 0 \\ 0 & 0 & 3 \end{pmatrix};$$

[111] orientation:

$$\overleftrightarrow{T}_1=\frac{1}{6}\begin{pmatrix} 3 & 0 & 0 \\ 0 & 3 & 0 \\ 0 & 0 & 0 \end{pmatrix},$$

$$\overleftrightarrow{T}_{2,3}=\frac{1}{6}\begin{pmatrix} 7/3 & \pm\sqrt{4/3} & \sqrt{2}/3 \\ \pm\sqrt{4/3} & 1 & \mp\sqrt{2/3} \\ \sqrt{2}/3 & \mp\sqrt{2/3} & 8/3 \end{pmatrix}, \tag{A3}$$

$$\overleftrightarrow{T}_4=\frac{1}{6}\begin{pmatrix} 1/3 & 0 & -\sqrt{8}/3 \\ 0 & 3 & 0 \\ -\sqrt{8}/3 & 0 & 8/3 \end{pmatrix}.$$

[1] Z. C. Feng, S. Perkowitz, and O. K. Wu, Phys. Rev. B **41**, 6057 (1990).

[2] B. G. Potter, Jr. and J. H. Simmons, Phys. Rev. B **43**, 2234 (1991).

[3] H. Pascher and G. Bauer, in *High Magnetic Fields in Semiconductor Physics*, edited by G. Landwehr, Springer Series in Solid-State Sciences Vol. 71 (Springer, Berlin, 1987), p. 400.

[4] F. Geist, H. Pascher, N. Frank, G. Bauer, and M. Kriechbaum, in *Proceedings of the 21st International Conference on the Physics of Semiconductors, Beijing, 1992*, edited by P. Jiang and H. Zheng (World Scientific, Singapore, 1992), p. 1928.

[5] J. C. Tsang, S. S. Iyer, J. A. Calise, and B. A. Ek, Phys. Rev. B **40**, 5886 (1989).

[6] P. A. M. Rodrigues, M. A. Araújo Silva, and F. Cerdeira, Phys. Rev. B **48**, 18 024 (1993).

[7] Shalini Ashokan, K. P. Jain, M. Balkanski, and C. Julien, Phys. Rev. B **44**, 11 133 (1991).

[8] R. K. Soni, S. Emura, K. Asami, and S. I. Gonda, in *Proceedings of the 21st International Conference on the Physics of Semiconductors, Beijing, 1992* (Ref. 4), p. 887.

[9] O. Günther, C. Janowitz, G. Jungk, B. Jenichen, R. Hey, L. Däweritz, and K. Ploog, Phys. Rev. B **52**, 2599 (1995).

[10] R. Dornhaus and G. Nimtz, in *Narrow-Gap Semiconductors*, edited by G. Höhler, Springer Tracts in Modern Physics Vol. 98 (Springer, Berlin, 1983), p. 119, and references therein.

[11] M. Lannoo and P. Friedel, in *Atomic and Electronic Structure of Surfaces*, Springer Series in Surface Sciences Vol. 16 (Springer, Berlin, 1991), p. 170.

[12] D. J. Chadi, J. P. Walter, M. L. Cohen, Y. Petroff, and M. Balkanski, Phys. Rev. B **5**, 3058 (1972).

[13] S. Katsuki and M. Kunimune, J. Phys. Soc. Jpn. **31**, 415 (1971).
[14] F. Stern and W. E. Howard, Phys. Rev. **163**, 816 (1967).
[15] M. Ritze and R. Enderlein, J. Cryst. Growth **101**, 359 (1990).
[16] M. Rösch, R. Atzmüller, G. Schaack, and C. R. Becker, Phys. Rev. B **49**, 13 460 (1994).
[17] L. He, C. R. Becker, R. N. Bicknell-Tassius, S. Scholl, and G. Landwehr, J. Appl. Phys. **73**, 3305 (1993).
[18] C. R. Becker, L. He, M. M. Regnet, M. M. Kraus, Y. S. Wu, G. Landwehr, X. F. Zhang, and H. Zhang, J. Appl. Phys. **74**, 2486 (1993).
[19] Y. Kim, A. Ourmazd, M. Bode, and R. D. Feldman, Phys. Rev. Lett. **63**, 636 (1989).
[20] F. Goschenhofer, V. Latussek, S. Einfeldt, M. O. Möller, C. R. Becker, and G. Landwehr, in *Proceedings of the 7th International Conference on Narrow-Gap Semiconductors, Santa Fe, 1995*, edited by J. L. Reno, IOP Conf. Proc. No. 144 (Institute of Physics and Physical Society, Bristol, 1995), p. 55.
[21] G. Bastard, *Wave Mechanics Applied to Semiconductor Heterostructures* (Les Editions de Physique, Les Ulis, 1988).
[22] K. Huang, B. Zhu, and H. Tang, Phys. Rev. B **41**, 5825 (1990).
[23] M. Cardona, in *Light Scattering in Solids II*, edited by M. Cardona and G. Güntherodt, Topics in Applied Physics Vol. 50 (Springer, Berlin, 1982), p. 19.
[24] A. K. Ganguly and J. L. Birman, Phys. Rev. **162**, 806 (1967).
[25] W. Limmer, Ph. D. thesis, Universität Regensburg, 1988.
[26] A. A. Gogolin and E. I. Rashba, Solid State Commun. **19**, 1077 (1976).
[27] W. Pötz and P. Vogl, Phys. Rev. B **24**, 2025 (1981).
[28] A. K. Sood, J. Menéndez, M. Cardona, and K. Ploog, Phys. Rev. Lett. **54**, 2111 (1985).
[29] B. Jusserand and M. Cardona, in *Light Scattering in Solids V*, edited by M. Cardona and G. Güntherodt, Topics in Applied Physics Vol. 66 (Springer, Berlin, 1989), p. 49.
[30] W. Richter, R. Zeyher, and M. Cardona, Phys. Rev. B **18**, 4312 (1978).
[31] E. O. Kane, Phys. Rev. **178**, 1368 (1969).
[32] E. O. Kane, Phys. Rev. **180**, 852 (1969).
[33] W. Kauschke, N. Mestres, and M. Cardona, Phys. Rev. B **36**, 7469 (1987).
[34] P. Manuel, G. A. Sai-Halasz, L. L. Chang, C. A. Chang, and L. Esaki, Phys. Rev. Lett. **37**, 1701 (1976).
[35] A. Lusson, J. Wagner, and M. Ramsteiner, Appl. Phys. Lett. **54**, 1787 (1989).
[36] R. Lassnig, Phys. Rev. B **30**, 7132 (1984).
[37] A. K. Arora, A. K. Ramdas, M. R. Melloch, and N. Otsuka, Phys. Rev. B **36**, 1021 (1987).
[38] Z. W. Fu and J. D. Dow, Phys. Rev. B **36**, 7625 (1987).
[39] D. N. Talwar and M. Vandevyver, J. Appl. Phys. **56**, 1601 (1984).
[40] M. Ritze (private communication).
[41] C. Tejedor, J. M. Calleja, F. Meseguer, E. E. Mendez, C. A. Chang, and L. Esaki, Phys. Rev. B **32**, 5303 (1985).
[42] A. Tardot, A. Hamoudi, N. Magnea, P. Gentile, and J. L. Pautrat, Appl. Phys. Lett. **62**, 2548 (1993).
[43] In Ref.16, Eq. (15), the matrix element $(\vec{\vec{T}}_4)_{23}$ has to be corrected to $+1$.